Supplementary Materials for

Fine dust emissions from active sands coastal Oceano Dunes, California

This file includes:

- Supplementary Methods
- Table S1. Heights of the four optical particle counters (OPCs) above the surface during the Oceano Dunes campaign.
- Table S2. 35 groups of calibration factors including the best-fit intercept a, uncertainty of intercept σ_a, slope b, uncertainty of slope σ_b and square of covariance ${\sigma_{ab}}^2$ for the measured aerosol number concentration of each bin of the five optical particle counters (OPCs).
- Fig. S1. Dust emission from Oceano Dunes during the same saltation event (A) at 2:36 pm on June 2nd, 2015 when saltation was weak, and (B) at 4:57 pm on June 2nd, 2015 when saltation was strong.
- Fig. S2. The experimental configuration of the five optical particle counters (OPCs) at the same height (1.95 meters) above the surface and in a line perpendicular to the wind during June 5th, 6th and 7th, 2015, collecting aerosol mass concentrations for OPC intercalibration.
- Fig. S3. Calibrated aerosol number concentration against uncalibrated concentration for each of the seven size bins (A) during June 5th to 7th, 2015 and (B) during May 29th to June 4th, 2015.
- Fig. S4. The ratio of scattered light intensity to incident intensity, $C_{sca} \int P_{11}(\Theta)$, as a function of particle diameter using Lorenz-Mie theory.
- Fig. S5. Aerosol mass concentration profiles during May 29th to June 4th, 2015 in order of increasing shear velocity.
- Fig. S6. The normalized volume size distribution of aerosol measured at the four OPC heights during May 29th to June 4th, 2015, (A) when saltation is inactive and (B) when saltation is active.
- Fig. S7. Vertical aerosol mass flux as a function of shear velocity calculated by using two plans of OPCs' assemblies during May 29th to June 4th, 2015: (A) using D1 and D2 only, and (B) using D3 and D4 only.
- Fig. S8. Vertical aerosol mass flux (using D1 and D2 only) as a function of shear velocity during May 29th to June 4th, 2015 using two regression methods: (A) sea-salt deposition flux is invariant with shear velocity, and (B) sea-salt deposition flux increases non-linearly with shear velocity.
- Fig. S9. The normalized volume size distribution of dust at emission using the mass flux calculated by the two regression methods.

Supplementary Methods

Overview

In this document, we present detailed descriptions of the intercalibration and error analysis on the five optical particle counters (OPCs) in Section 1, the correction on the OPC bin sizes using Lorenz-Mie theory in Section 2, the regression on the vertical profiles of aerosol mass concentrations in Section 3, and the methodology to remove the effect of sea-salt deposition flux on these profiles in Section 4.

1. Intercalibration and error analysis on the five optical particle counters (OPCs)

1.1 Two periods of OPC configurations

We used six identical OPCs (with Series ID 9284, 9290, 9281, 9278, 9287 and 9286, respectively) in the Oceano Dunes field campaign from May 15th to June 7th, 2015. Because OPC 9286 broke on May 25th and therefore could not be included in the subsequent calibration activity, we did not use measurements of this sensor for all of our subsequent analysis. During May 26th to June 4th, 2015, we obtained vertical aerosol number concentrations using four OPCs (of the five good ones) mounted at four different heights at any given time (Table S1 and Fig. 1). During June 5th to June 7th, 2015, we mounted the five good OPCs at the same height and in a line perpendicular to the wind (Fig. S2). The first configuration (May 26th – June 4th) was used to measure fluxes of dust emission, whereas the second configuration (June 5th – 7th) was used to intercalibrate the five OPCs.

1.2 Data-quality control criteria

For the first configuration (May 26th – June 4th), we had three data-quality control criteria. After we built 30-minute time blocks and assigned each one second-averaged measurement of aerosol concentration into its corresponding time block, (1) we eliminated those blocks containing fewer than 1800 valid data points (i.e., 30 minutes * 60 second-averaged measurements per minute), (2) we eliminated those blocks with their mean wind directions outside of $\pm$45 degrees relative to the daily mean wind (Martin and Kok, 2017; Martin et al., 2018), and (3) we eliminated those blocks from May 26th to May 28th, during which the heights of the four OPC sensors were not consistent with the other blocks after May 29th (Table S1) such that these heights were not appropriate for subtracting sea-salt deposition flux in a consistent way. For the second (intercalibration) configuration (June 5th – 7th), we only applied the first quality control criterion, because we were not considered with obtaining vertical profiles for dust flux calculations.

1.3 Intercalibration of the five OPCs during June 5th to 7th

During the second configuration (June 5th to 7th, 2015), the five OPCs were set at the same height to measure aerosol concentrations simultaneously (Fig. S2). For each of the seven size bins (we ignored the largest bin #8 due to insufficient particle counts for constraining uncertainty), we applied linear-least squares regression on aerosol concentration of each of the five OPCs against the mean of the five OPCs, and obtained a correction factor with uncertainty for each OPC (Table S2 and Fig. S3).

Specifically, for each of the seven size bins, we used the following equation to obtain the best-fit intercept and slope for each OPC with respect to the mean value of the five OPCs,

$$\ln(y_j) = a_{i,j} + b_{i,j} \cdot \ln(x_{i,j}), \quad \text{(S1.1)}$$

where the subscripts $i = 1, 2, \dots, 5$ refer to individual OPCs, $j = 1, 2, \dots, 7$ refer to individual size bin, y_j (in the unit of $\#/\mathrm{m}^3$) is the mean concentration of the five OPCs for bin j, and $x_{i,j}$ (in the unit of $\#/\mathrm{m}^3$) is the concentration of each of the five OPCs for bin j. To simplify the following regression procedure, we define

$$u_j = \ln(y_j), \quad \text{(S1.2)}$$

$$v_{i,j} = \ln(x_{i,j}), \quad \text{(S1.3)}$$

such that Eq. (S1.1) converts into

$$u_j = a_{i,j} + b_{i,j} * v_{i,j} \quad \text{(S1.4).}$$

We used the linear-least squares regression to find the best-fit intercept a, slope b, their uncertainties σ_a and σ_b and covariance σ_{ab} by (Bevington and Robinson, 2003),

$$a_{i,j} = \frac{1}{\Delta_{i,j}}\left(\sum_{k=1}^{N_{i,j}} {v_{i,j,k}}^2 \sum_{k=1}^{N_{i,j}} u_{j,k} - \sum_{k=1}^{N_{i,j}} v_{i,j,k} \sum_{k=1}^{N_{i,j}} v_{i,j,k} u_{j,k}\right), \quad \text{(S1.5)}$$

$$b_{i,j} = \frac{1}{\Delta_{i,j}}\left(N_{i,j} \sum_{k=1}^{N_{i,j}} v_{i,j,k} u_{j,k} - \sum_{k=1}^{N_{i,j}} v_{i,j,k} \sum_{k=1}^{N_{i,j}} u_{j,k}\right), \quad \text{(S1.6)}$$

$$\Delta_{i,j} = N_{i,j} \sum_{k=1}^{N_{i,j}} {v_{i,j,k}}^2 - \left(\sum_{k=1}^{N_{i,j}} v_{i,j,k}\right)^2, \quad \text{(S1.7)}$$

$${\sigma_{a,i,j}}^2 = \frac{{\sigma_{i,j}}^2}{\Delta_{i,j}} \sum_{k=1}^{N_{i,j}} {v_{i,j,k}}^2, \quad \text{(S1.8)}$$

$${\sigma_{b,i,j}}^2 = \frac{N_{i,j} {\sigma_{i,j}}^2}{\Delta_{i,j}}, \quad \text{(S1.9)}$$

$${\sigma_{ab,i,j}}^2 = \sum_{k=1}^{N_{i,j}} \left({\sigma_{i,j}}^2 \frac{\partial a_{i,j}}{\partial u_{j,k}} \frac{\partial b_{i,j}}{\partial u_{j,k}}\right), \quad \text{(S1.10)}$$

$${\sigma_{i,j}}^2 = \frac{1}{N_{i,j} - 2} \sum_{k=1}^{N_{i,j}} \left(u_{j,k} - a_{i,j} - b_{i,j} * v_{i,j,k}\right)^2, \quad \text{(S1.11)}$$

$$\frac{\partial a_{i,j}}{\partial u_{j,k}} = \frac{1}{\Delta_{i,j}}\left(\sum_{k=1}^{N_{i,j}} {v_{i,j,k}}^2 - v_{i,j,k} \sum_{k=1}^{N_{i,j}} v_{i,j,k}\right), \quad \text{(S1.12)}$$

$$\frac{\partial b_{i,j}}{\partial u_{j,k}} = \frac{1}{\Delta_{i,j}} \left(N_{i,j} v_{i,j,k} - \sum_{k=1}^{N_{i,j}} v_{i,j,k} \right) \quad \text{(S1.13).}$$

where the subscript $k = 1, 2, \ldots, N_{i,j}$ is individual measurement, $N_{i,j}$ is the number of individual measurements of the j^{th} size bin of the i^{th} OPC, $\sigma_{a,i,j}$ is the uncertainty of the intercept $a_{i,j}$, $\sigma_{b,i,j}$ is the uncertainty of the slope $b_{i,j}$, $\sigma_{ab,i,j}$ is the uncertainty of the covariance between the intercept $a_{i,j}$ and the slope $b_{i,j}$, ${\sigma_{i,j}}^2$ is the estimate of the variance in $u_{j,k}$, the partial derivatives $\frac{\partial a_{i,j}}{\partial u_{j,k}}$ and $\frac{\partial b_{i,j}}{\partial u_{j,k}}$ are the quantitative sensitivity of the parameters $a_{i,j}$ and $b_{i,j}$ to the value of each individual $v_{i,j,k}$.

Using the procedure above, we obtained 35 groups (5 OPCs * 7 bins) of calibration factors including the best-fit intercept a, slope b, their uncertainties σ_a and σ_b and covariance σ_{ab} (Table S2), based on which we generated regressed lines (solid lines in Fig. S3). We then derived the regressed uncertainty $\sigma_{fit,i,j}$ at a given point of the regressed line (dashed lines in Fig. S3) from error propagation on Eq. (S1.1) (p. 98-115 in Bevington and Robinson, 2003),

$$\sigma_{fit,i,j} = \sqrt{{\sigma_{a,i,j}}^2 \left(\frac{\partial y_j}{\partial a_{i,j}} \right)^2 + {\sigma_{b,i,j}}^2 \left(\frac{\partial y_j}{\partial b_{i,j}} \right)^2 + 2{\sigma_{ab,i,j}}^2 \left(\frac{\partial y_j}{\partial a_{i,j}} \right) \left(\frac{\partial y_j}{\partial b_{i,j}} \right)} =$$

$$\sqrt{{\sigma_{a,i,j}}^2 e^{2\ln(y_{j,k})} + {\sigma_{b,i,j}}^2 \left(e^{\ln(y_{j,k})} \cdot \ln\left(x_{i,j,k}\right) \right)^2 + 2{\sigma_{ab,i,j}}^2 \left(e^{2\ln(y_{j,k})} \cdot \ln\left(x_{i,j,k}\right) \right)} \quad \text{(S1.14).}$$

1.4 Calibration factors onto measurements during May 29th to June 4th

We applied the 35 groups of calibration factors (Table S2) on OPC measurements during May 29th to June 4th, 2015 by

$$y'_{i,j} = e^{a_{i,j} + b_{i,j} \cdot ln(x'_{i,j})} \quad \text{(S1.15)}$$

where $y'_{i,j}$ (in the unit of $\#/\text{m}^3$) is the calibrated aerosol concentration of the j^{th} bin of the i^{th} OPC during May 29th to June 4th, $x'_{i,j}$ (in the unit of $\#/\text{m}^3$) is the uncalibrated measurement, $a_{i,j}$ and $b_{i,j}$ are best-fit intercept and slope listed in Table S2. Similar to Eq. (S1.14), the regressed uncertainty was obtained by error propagation,

$$\sigma'_{fit,i,j} = \sqrt{{\sigma_{a,i,j}}^2 e^{2\ln(y'_{i,j,k})} + {\sigma_{b,i,j}}^2 \left(e^{\ln(y'_{i,j,k})} \cdot \ln\left(x'_{i,j,k}\right) \right)^2 + 2{\sigma_{ab,i,j}}^2 \left(e^{2\ln(y'_{i,j,k})} \cdot \ln\left(x'_{i,j,k}\right) \right)} \quad \text{(S1.16)}$$

where $y'_{i,j,k}$ (in the unit of $\#/\text{m}^3$) is the k^{th} calibrated aerosol concentration of the j^{th} bin of the i^{th} OPC, $x'_{i,j,k}$ (in the unit of $\#/\text{m}^3$) is the uncalibrated measurement, $\sigma_{a,i,j}$ $\sigma_{b,i,j}$ and ${\sigma_{ab,i,j}}^2$ are the calibration factors listed in Table S2.

Using the procedure above, we obtained the calibrated aerosol number concentration of each bin of the five OPCs in 30-minute intervals during May 29th to June 4th, 2015 by applying the calibration factors (Table S2) and acquired the regressed uncertainty range by error propagation (Fig. S3).

2. OPC bin size correction by Lorenz-Mie theory

Because the output size values from the OPCs were those of polystyrene latex spheres (PSLs) following the international standard ISO 21501-1:2009 (ISO, 2009), the OPCs were not internally calibrated to any particular dust mineralogy. The optical sizing of dust is sensitive to differences in the refractive index between dust and PSLs. As such, we corrected the manufacturer-provided bin sizes of PSLs to dust using Lorenz-Mie theory (Bohren and Huffman, 1983), thereby approximating dust as spherical particles.

Mätzler (2002) presented MATLAB code for Lorenz-Mie theory. The input variables include the particle complex refractive index m, wavelength in the ambient medium λ, and the particle geometric diameter d. The output variables, related to our calculation, include the scattering efficiency Q_{sca} and the two scattering amplitude functions $S_1(\Theta)$ and $S_2(\Theta)$. We applied the following equations on the MATLAB code outputs to obtain the phase function $P_{11}(\Theta)$, the scattering cross section C_{sca} (Eqs. (5.2.111a), (5.2.112a) and (5.2.94) of Liou, 2002)

$$P_{11}(\Theta) = \frac{4\pi}{2\left(\frac{2\pi}{\lambda}\right)^2 C_{sca}} \left(|S_1(\Theta)|^2 + |S_2(\Theta)|^2\right) \quad (S2.1)$$

$$C_{sca} = Q_{sca} \cdot \pi \left(\frac{d}{2}\right)^2 \quad (S2.2).$$

The phase function quantifies the angular distribution of scattered intensity and the scattering cross section quantifies the amount of energy scattered from the incident bean by a particle (Liou, 2002). Therefore, the scattered intensity I_s in Lorenz-Mie theory can be quantified by (Bohren and Huffman, 1983; Liou, 2002),

$$I_s(\Theta) = I_i \frac{C_{sca} P_{11}(\Theta)}{4\pi r^2} \quad (S2.3),$$

where r is the distance between the center of the particle to the receiver of the OPC and I_i is the incident intensity. The OPC measures scattered intensity within the scattering angle $\Theta = 90° \pm 60°$ (information provided by Met One Engineering Department). As such, the scattered intensity measured by OPC is

$$I_s(90° \pm 60°) = \frac{C_{sca} I_i}{4\pi r^2} \int_{30°}^{150°} P_{11}(\Theta) \sin(\Theta)\, d\Theta \quad (S2.4).$$

Although we do not know the value of r and I_i, they are constants and do not affect the calculations that follow. Therefore, we quantify the scattered intensity measured by OPC using

$$4\pi r^2 \frac{I_s(90° \pm 60°)}{I_i} = C_{sca} \int_{30°}^{150°} P_{11}(\Theta) \sin(\Theta)\, d\Theta \quad (S2.5).$$

Eq. (S2.5) thus establishes the link between C_{sca} ·integral$\left(P_{11}(\Theta)\right)$, the input complex refractive index m, the laser diode wavelength λ used by OPC, and the particle geometric diameter d.

We corrected the OPC bin sizes through two steps. We first input the manufacturer-provided eight bin boundary diameters (seven bins) of PSLs (Table 1, column 1) and their refractive index ($m = 1.59 - 0\text{i}$) into Eq. (S2.5), and output the corresponding C_{sca} ·integral$\left(P_{11}(\Theta)\right)$ for each of the eight bin boundary diameters. Second, we input a range of dust refractive indexes (real part $n = 1.53 \pm 0.03$ and imaginary part $k = -10^{-2.5\pm0.3}$, summarized in Kok et al., 2017) and an array of dust diameters into Eq. (S2.5). We determined the dust geometric diameters of the eight bin boundaries that produce the same C_{sca} ·integral$\left(P_{11}(\Theta)\right)$ as that of the eight manufacturer-provided PSLs bin boundary diameters calculated in step one (Table 1, column 2 and Fig. S4).

3. Concentration unit conversion and profile fitting

We generated the concentration profile in preparation for the dust flux calculation using the gradient method (Gillette et al., 1972; Shao, 2008). To obtain the concentration profile, we first converted the calibrated 30-minute aerosol number concentration at four different heights into mass concentrations, after which we fit regressions on the height-resolved mass concentrations.

We converted between the number concentration C_N ($\#/\text{m}^3$) and the mass concentration C_M (kg/m^3) as (Seinfeld and Pandis, 2016)

$$C_{M_{i,j}} = \frac{\rho}{6}\pi C_{N_{i,j}}\left(D_j \cdot 10^{-6}\right)^3, \quad \text{(S3.1)}$$

where the subscripts $i = 1, 2, \ldots, 4$ refer to the OPCs, $j = 1, 2, \ldots, 7$ refer to the size bins, $\rho = 2.5 \pm 0.2 \times 10^3\ \text{kg}/\text{m}^3$ is the dust density (Kok et al., 2017), and D_j (in the unit of μm) is the dust geometric diameters of the j^{th} bin (Table 1, column 2).

In order to obtain the size-resolved mass fluxes, we applied linear-least squares regression (Eq. (3)) to vertical mass concentration profiles for each of the seven size bins. As such, we obtained the concentration profile fits for each size bin associated with concurrent shear velocity measurements (in units of m/s) (Fig. S5).

4. Removal of sea-salt aerosol deposition signal from dust flux calculations

We found that the concentration profiles (Fig. S5) deviated from the logarithmic profiles expected to occur from an active emission source (Stull, 1988; Kind, 1992; Gillies and Berkofsky, 2004), a result that we inferred as the influence of sea-salt aerosol. Because we measured dust concentrations ~650 meters from the shoreline, we expect increasing sea-salt aerosol concentration with height due to the upwind deposition of near-surface sea-salt aerosol (Liang et al., 2016). We indeed generally observed an increasing concentration with height for the lowest two or three OPCs when saltation was inactive (horizontal saltation flux $Q = 0$), consistent with sea-salt deposition, but found a decrease in concentration with height when saltation was active ($Q > 0$), consistent with dust emission (Fig. S5). In this section, we describe (1) how we diagnosed whether sea-salt aerosols played a role and (2) how we removed their effect on our measurements to the extent possible.

4.1 Diagnosis of sea-salt aerosols deposition

We calculated the normalized volume size distribution of the four OPC heights (Table S1) during May 29th to June 4th, 2015 separately for times when saltation is inactive (Fig. S6A) and active (Fig. S6B). The aerosol PSD when saltation is inactive is largely coarser than when it is active for all four heights. Because sea-salt aerosols are significantly coarser than dust (O'Dowd and de Leeuw, 2007), we concluded that sea-salt deposition affected our measurements at all four heights.

Because lower sensors more strongly reflect local dust emission whereas the higher sensors reflect the upwind signal from the sea-salt deposition, we used partial of the four OPCs to study the contribution of sea-salt aerosols deposition to the dust emission measurements. Specifically, we studied two types of measured concentration profiles to calculate the vertical mass flux: (1) using only D1 and D2 and (2) only D3 and D4 (detailed heights of D1, D2, D3 and D4 are listed in Table S1).

Because deposition of sea-salt aerosols leads to negative vertical mass flux ($F_d < 0$) and emission of dust aerosols leads to positive mass flux ($F_d > 0$), we used the difference in the sign of mass flux to distinguish the contributions of sea-salt aerosols versus dust aerosols. Specifically, for each of the two plans mentioned in the previous paragraph, we categorized the gradient-method calculated mass fluxes (Eq. (3)) into four scenarios: (1) active saltation and positive vertical mass flux ($Q > 0, F_d > 0$), (2) active saltation and negative vertical mass flux ($Q > 0, F_d < 0$), (3) inactive saltation and positive vertical mass flux ($Q = 0, F_d > 0$) and (4) inactive saltation and negative mass flux ($Q = 0, F_d < 0$).

Fig. S7 shows the results of the four scenarios for the two plans. Using only the lowest two OPCs, D1 and D2, we found the aerosol flux to be small and negative (deposition) when saltation was inactive, and large and positive (emission) when saltation was active. In contrast, use of the higher OPCs, D3 and D4, showed a positive aerosol flux when saltation was inactive, which indicated a large dust signal pollution by sea-salt aerosols. This comparison in the two plans supports that lower sensors more strongly reflect local dust emission whereas the higher sensors reflect the upwind signal from the sea-salt deposition (refer to saltation layer height detailed in Martin and Kok, 2017). As such, we used only D1 and D2 to calculate the dust emission flux.

4.2 Two regression methods to remove sea-salt deposition flux

Because using only the lowest two OPCs did not eliminate the deposition flux of sea-salt from our results, we subtracted mass fluxes measured by D1 and D2 during inactive saltation events (inferred as the background sea-salt deposition signal) from the mass fluxes calculated by D1 and D2 during active saltation events. Since we were unable to find independent detailed *in situ* measurements relating near-shore sea-salt deposition flux to shear velocity (u_*), we considered two different empirical regression methods to correct for the background sea-salt deposition signal: (1) sea-salt deposition flux is invariant with increasing shear velocity and (2) sea-salt deposition flux increases non-linearly with increasing shear velocity. Fig. S8 shows the results of the two regression methods.

After we obtained the regressed absolute value of the sea-salt deposition flux during active saltation (red regression lines in Fig. S8), we added the regressed deposition fluxes (i.e., subtracted the equivalent emission values) from the calculated mass fluxes during active saltation (red closed left-pointing triangles in Fig. S8). The summed values are the net dust emission fluxes during active saltation events.

We compared the PSD of emitted dust obtained by the two regression methods (Fig. S9). Because the second regression method leads to a decreasing trend of mass flux with increasing shear velocity (Bin #2, 3, and 4 in Fig. S8B) and the PSDs of emitted dust obtained by the two regression methods are highly similar (Fig. S9), we chose to use the simpler correction assuming a constant sea-salt deposition flux for obtaining the net dust deposition fluxes presented in the main text.

5. References:

Bevington, P. R. and Robinson, D. K.: Data reduction and error analysis for the physical sciences, 3rd ed., McGraw-Hill Education., 2003.

Bohren, C. F. and Huffman, D. R.: Absorption and scattering of light by small particles, 1st ed., Wiley-VCH., 1983.

Gillette, D. A., Blifford, I. H. and Fenster, C. R.: Measurements of aerosol size distributions and vertical fluxes of aerosols on land subject to wind erosion, J. Appl. Meteorol. Climatol., 11(6), 977–987, doi:10.1175/1520-0450(1972)011<0977:MOASDA>2.0.CO;2, 1972.

Gillies, J. A. and Berkofsky, L.: Eolian suspension above the saltation layer, the concentration profile, J. Sediment. Res., 74(2), 176–183, doi:10.1306/091303740176, 2004.

ISO: Determination of particle size distribution: single particle light interaction methods, part 1: Light scattering aerosol spectrometer, ISO 21501-1, 2009.

Kind, R. J.: One-dimensional aeolian suspension above beds of loose particles-A new concentration-profile equation, Atmos. Environ., 26A(5), 927–931, doi:10.1016/0960-1686(92)90250-O, 1992.

Kok, J. F., Ridley, D. A., Zhou, Q., Miller, R. L., Zhao, C., Heald, C. L., Ward, D. S., Albani, S. and Haustein, K.: Smaller desert dust cooling effect estimated from analysis of dust size and abundance, Nat. Geosci., 10(March), doi:10.1038/ngeo2912, 2017.

Liang, T., Chamecki, M. and Yu, X.: Sea salt aerosol deposition in the coastal zone: A large eddy simulation study, Atmos. Res., 180, 119–127, doi:10.1016/j.atmosres.2016.05.019, 2016.

Liou, K.-N.: An introduction to atmospheric radiation, 2nd ed., Academic Press, Inc., 2002.

Martin, R. L., Kok, J. F., Hugenholtz, C. H., Barchyn, T. E., Chamecki, M. and Ellis, J. T.: High-frequency measurements of aeolian saltation flux: Field-based methodology and applications, Aeolian Res., 30, 97–114, doi:10.1016/j.aeolia.2017.12.003, 2018.

Martin, R. L. and Kok, J. F.: Wind-invariant saltation heights imply linear scaling of aeolian saltation flux with shear stress, Sci. Adv., 3(6), 1–30, doi:10.1126/sciadv.1602569 ., 2017.

Mätzler, C.: MATLAB Functions for Mie Scattering and Absorption, version 2, IAP Res. Rep., 1–24, doi:10.1039/b811392k, 2002.

O'Dowd, C. D. and de Leeuw, G.: Marine aerosol production: a review of the current knowledge, Philos. Trans. R. Soc. A Math. Phys. Eng. Sci., 365(1856), 1753–1774, doi:10.1098/rsta.2007.2043, 2007.

Seinfeld, J. H. and Pandis, S. N.: Atmospheric chemistry and physics: from air pollution to climate change, 3rd ed., Wiley., 2016.

Shao, Y.: Physics and modelling of wind erosion, 2nd ed., edited by Y. Shao, Springer, Netherlands., 2008.

Stull, R. B.: An introduction to boundary layer meteorology, 1st ed., Springer Netherlands., 1988.

Tables and Figures

Table S1. Heights of the four optical particle counters (OPCs) above the surface during the Oceano Dunes campaign. D1 denotes the OPC set at the lowest height, D2 the second lowest, D3 the third lowest and D4 at the highest height (see Fig. 1).

Measurement Time (Pacific Time) (Month-Day Start Time- End Time)		D1 (m)	D2 (m)	D3 (m)	D4 (m)
05-15 13:03- 18:14		1.62	3.54	6.44	None
05-16 10:48- 17:47		1.62	3.54	6.44	None
05-19 13:50- 15:18		1.62	2.74	3.54	None
05-23 12:24- 18:28		1.62	2.74	3.54	6.44
05-24	11:27- 12:37	1.62	2.74	3.54	6.44
	13:08- 16:40	1.62	2.74	6.44	None
05-26 13:07- 18:01		1.11	1.62	2.74	6.44
05-27 12:04- 18:01		1.11	1.62	2.74	6.44
05-28 12:20- 17:32		1.11	1.62	2.74	6.44
05-29 11:22- 17:08		0.74	1.48	2.29	6.44
05-30 10:16- 18:16		0.74	1.48	2.29	6.44
05-31 10:03- 18:01		0.74	1.48	2.29	6.44
06-01 10:26- 15:35		0.74	1.48	2.29	6.44
06-02 10:47- 18:14		0.75	1.49	2.31	6.44
06-03 11:57- 18:36		0.75	1.49	2.30	6.44
06-04 11:24- 15:22		0.75	1.49	2.31	6.44

Table S2. 35 groups of calibration factors including the best-fit intercept a, uncertainty of intercept σ_a, slope b, uncertainty of slope σ_b and square of covariance ${\sigma_{ab}}^2$ for the measured aerosol number concentration of each bin of the five optical particle counters (OPCs). These regression constants are obtained using the linear-least squares regression method.

OPC Series ID		$a \pm \sigma_a$	$b \pm \sigma_b$	${\sigma_{ab}}^2$
9284	Bin_1	0.1485 $\pm$ 0.3228	0.9850 $\pm$ 0.0511	-0.0165
	Bin_2	0.0463 $\pm$ 0.4775	1.0110 $\pm$ 0.0811	-0.0387
	Bin_3	-0.1671 $\pm$ 0.6240	1.0506 $\pm$ 0.1112	-0.0693
	Bin_4	0.0320 $\pm$ 0.6623	1.0146 $\pm$ 0.1292	-0.0855
	Bin_5	0.4924 $\pm$ 0.5089	0.9251 $\pm$ 0.1089	-0.0554
	Bin_6	1.3569 $\pm$ 0.4838	0.7427 $\pm$ 0.1324	-0.0639
	Bin_7	1.9912 $\pm$ 0.3033	0.5138 $\pm$ 0.1138	-0.0342
9290	Bin_1	0.1391 $\pm$ 0.3233	0.9799 $\pm$ 0.0508	-0.0164

	Bin_2	0.2129 ± 0.4656	0.9709 ± 0.0782	-0.0364
	Bin_3	0.2331 ± 0.5881	0.9693 ± 0.1037	-0.0609
	Bin_4	0.1176 ± 0.6682	0.9853 ± 0.1287	-0.0860
	Bin_5	0.0669 ± 0.5774	0.9881 ± 0.1202	-0.0694
	Bin_6	0.4025 ± 0.7106	0.9079 ± 0.1760	-0.1249
	Bin_7	0.6305 ± 0.5245	0.8126 ± 0.1563	-0.0818
9281	Bin_1	0.1524 ± 0.3216	0.9965 ± 0.0515	-0.0166
	Bin_2	0.0752± 0.4729	1.0190 ± 0.0814	-0.0385
	Bin_3	-0.0575 ± 0.6124	1.0569 ± 0.1118	-0.0685
	Bin_4	0.4705 ± 0.6113	0.9506 ± 0.1220	-0.0746
	Bin_5	0.7238 ± 0.4814	0.8861± 0.1043	-0.0502
	Bin_6	1.3071 ± 0.4939	0.7385 ± 0.1320	-0.0651
	Bin_7	1.8436 ± 0.2680	0.5393 ± 0.0950	-0.0252
9278	Bin_1	-0.1650 ± 0.3384	1.0092 ± 0.0522	-0.0177
	Bin_2	-0.1400 ± 0.4896	0.9987 ± 0.0797	-0.0390
	Bin_3	-0.0487 ± 0.6072	0.9759 ± 0.1025	-0.0622
	Bin_4	-0.0345 ± 0.6741	0.9683 ± 0.1239	-0.0835
	Bin_5	-0.2932 ± 0.6063	1.0223 ± 0.1214	-0.0736
	Bin_6	-0.4668 ± 0.8268	1.0350 ± 0.1887	-0.1559
	Bin_7	-0.3394 ± 0.6523	0.9947 ± 0.1756	-0.1143
9287	Bin_1	-0.0045 ± 0.3301	0.9928 ± 0.0514	-0.0170
	Bin_2	0.1136 ± 0.4699	0.9656 ± 0.0771	-0.0362
	Bin_3	0.2728 ± 0.5741	0.9369 ± 0.0985	-0.0565
	Bin_4	0.2557 ± 0.6319	0.9441 ± 0.1199	-0.0757
	Bin_5	0.3338 ± 0.5252	0.9201 ± 0.1078	-0.0566
	Bin_6	0.1567 ± 0.7051	0.9496 ± 0.1711	-0.1205
	Bin_7	0.2439 ± 0.5531	0.9123 ± 0.1621	-0.0894

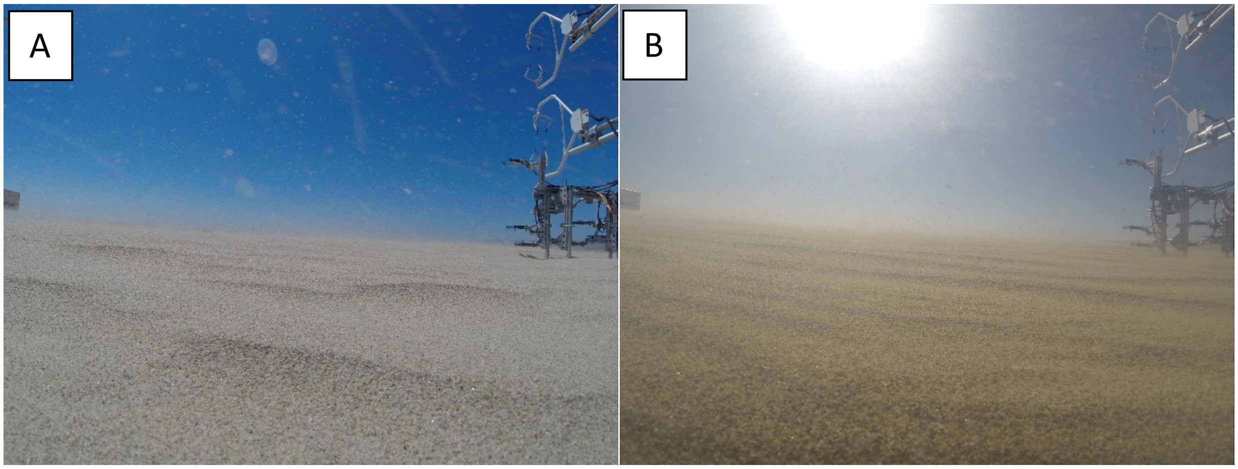

Figure S1. Dust emission from Oceano Dunes during the same saltation event (A) at 2:36 pm on June 2nd, 2015 when saltation was weak, and (B) at 4:57 pm on June 2nd, 2015 when saltation was strong. The two sonic anemometers in the top right corner are located at 0.64 meters and 1.16 meters above the surface. Although sun glare obscures (B), the increase in haziness in the upper half of the photograph suggests active dust emission from the study site.

Figure S2. The experimental configuration of the five optical particle counters (OPCs) (with Series ID 9284, 9290, 9281, 9278 and 9287, respectively) at the same height (1.95 meters) above the surface and in a line perpendicular to the wind during June 5th, 6th and 7th, 2015, collecting aerosol number concentrations for OPC intercalibration.

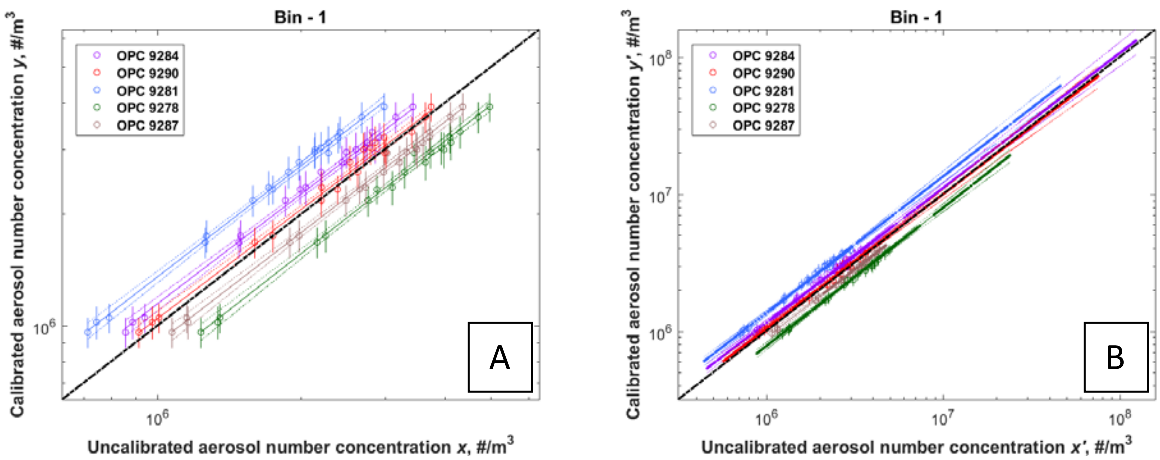
Bin - 1
OPC 9284
OPC 9290
OPC 9281
OPC 9278
OPC 9287
Calibrated aerosol number concentration y, #/m^3
Uncalibrated aerosol number concentration x, #/m^3
A
Bin - 1
Calibrated aerosol number concentration y', #/m^3
Uncalibrated aerosol number concentration x', #/m^3
B

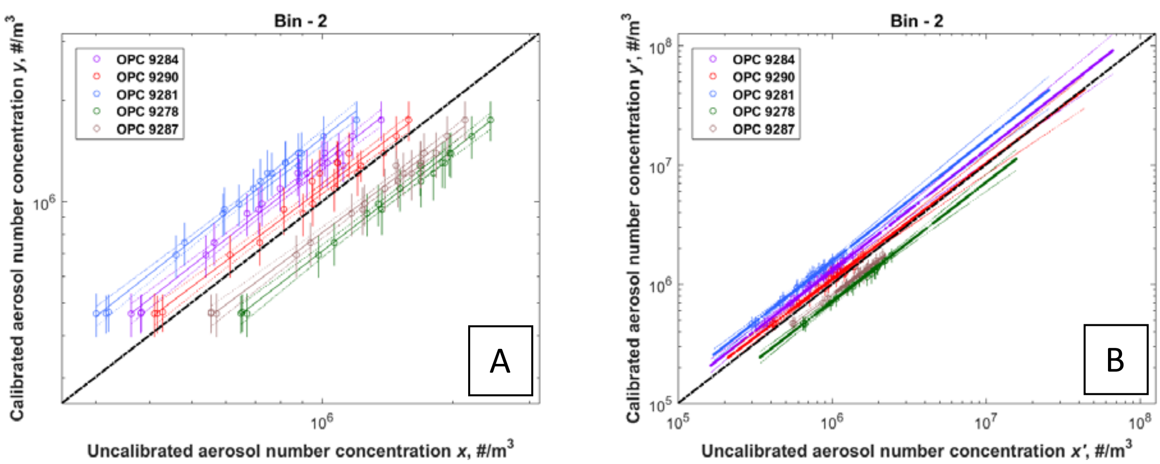
Bin - 2
OPC 9284
OPC 9290
OPC 9281
OPC 9278
OPC 9287
Calibrated aerosol number concentration y, #/m^3
Uncalibrated aerosol number concentration x, #/m^3
A
Bin - 2
Calibrated aerosol number concentration y', #/m^3
Uncalibrated aerosol number concentration x', #/m^3
B

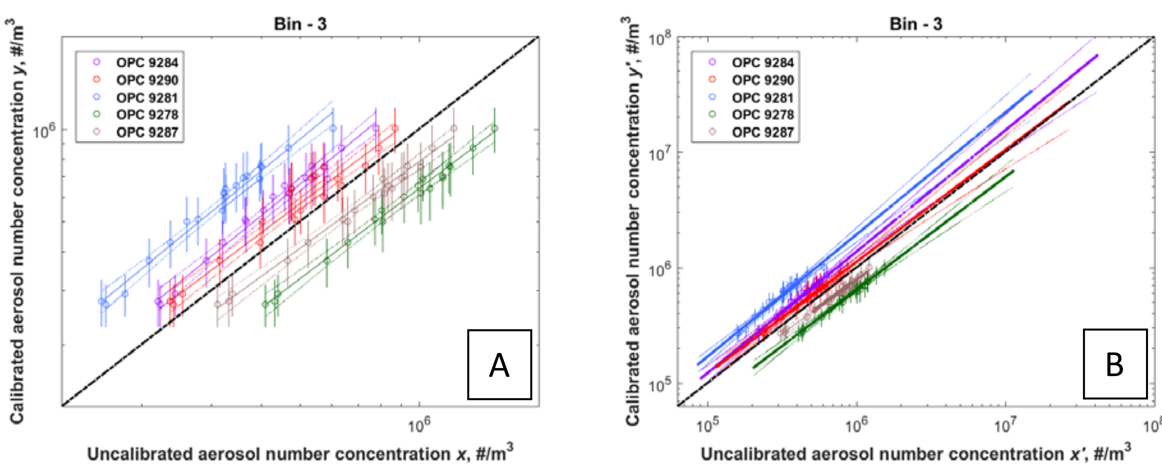
Bin - 3
OPC 9284
OPC 9290
OPC 9281
OPC 9278
OPC 9287
Calibrated aerosol number concentration y, #/m^3
Uncalibrated aerosol number concentration x, #/m^3
A
Bin - 3
Calibrated aerosol number concentration y', #/m^3
Uncalibrated aerosol number concentration x', #/m^3
B

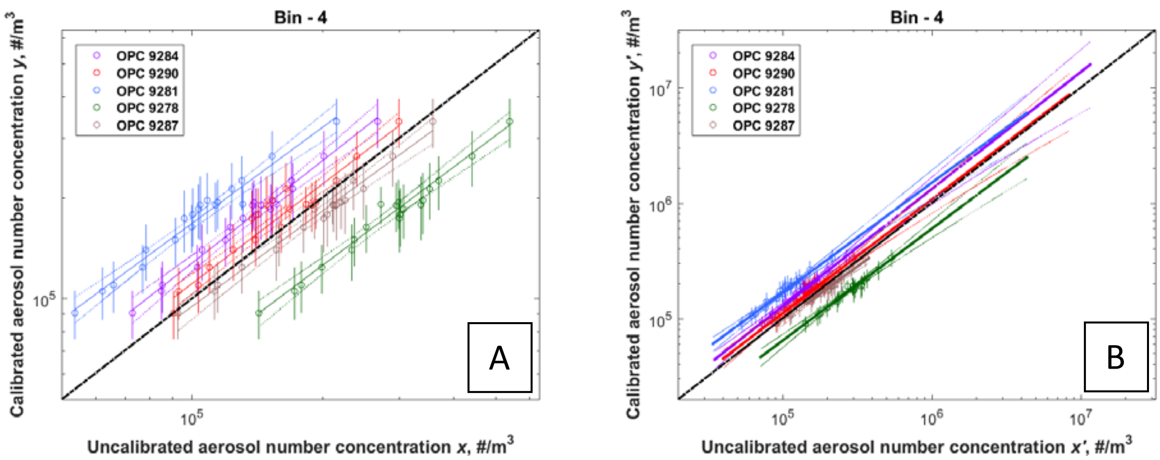
Bin - 4
OPC 9284
OPC 9290
OPC 9281
OPC 9278
OPC 9287
A
B
Calibrated aerosol number concentration y, #/m3
Uncalibrated aerosol number concentration x, #/m3
Calibrated aerosol number concentration y', #/m3
Uncalibrated aerosol number concentration x', #/m3

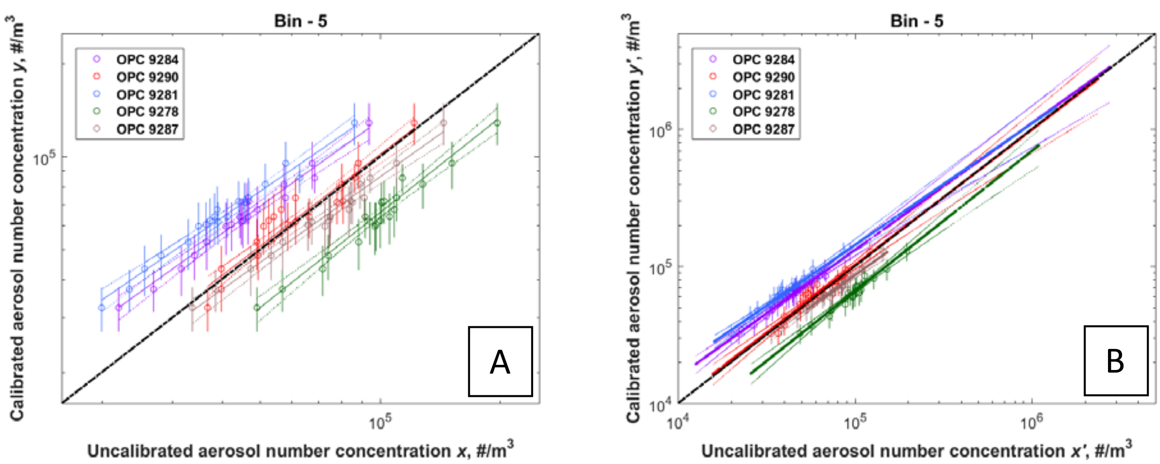
Bin - 5
OPC 9284
OPC 9290
OPC 9281
OPC 9278
OPC 9287
A
B
Calibrated aerosol number concentration y, #/m3
Uncalibrated aerosol number concentration x, #/m3
Calibrated aerosol number concentration y', #/m3
Uncalibrated aerosol number concentration x', #/m3

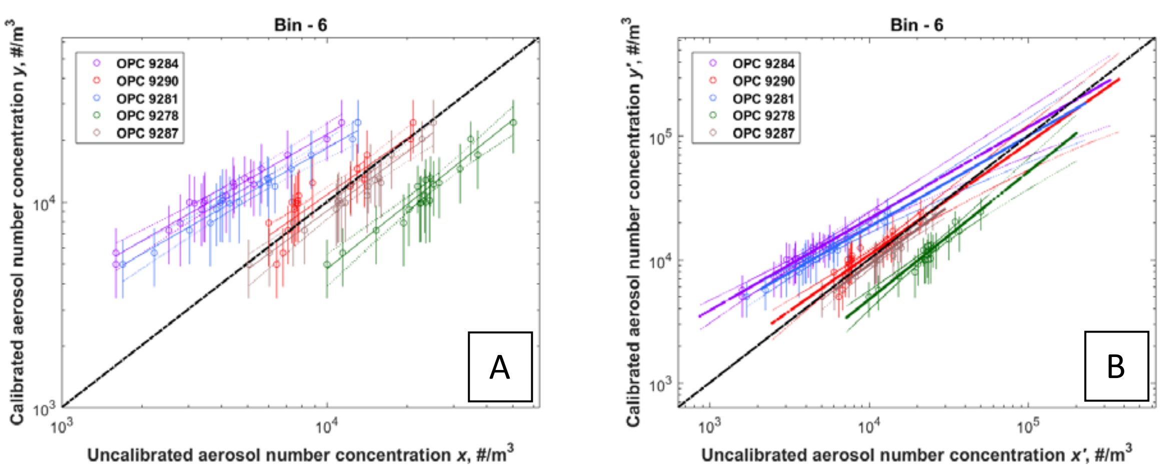
Bin - 6
OPC 9284
OPC 9290
OPC 9281
OPC 9278
OPC 9287
A
B
Calibrated aerosol number concentration y, #/m3
Uncalibrated aerosol number concentration x, #/m3
Calibrated aerosol number concentration y', #/m3
Uncalibrated aerosol number concentration x', #/m3

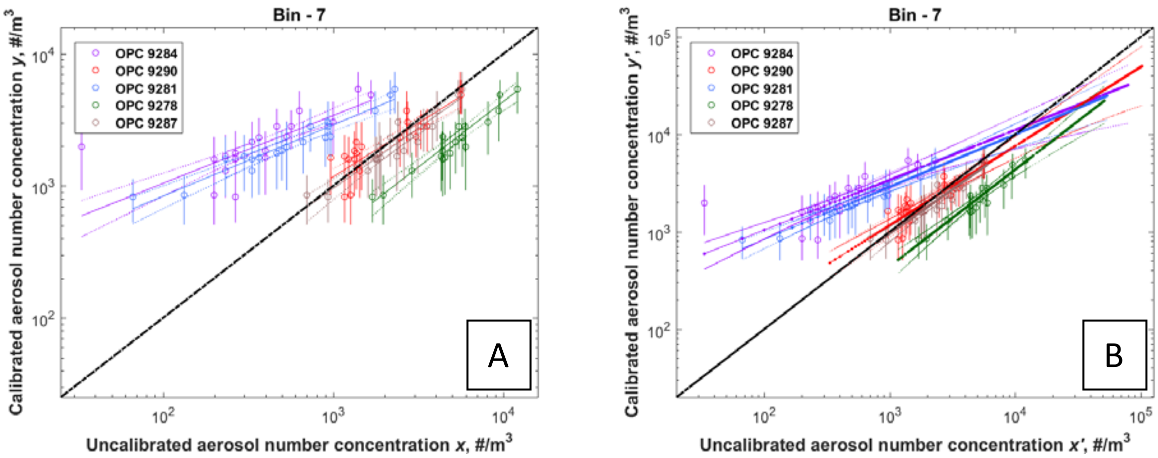

Figure S3. Calibrated aerosol number concentration against uncalibrated concentration for each of the seven size bins (A) during June 5th to 7th, 2015 and (B) during May 29th to June 4th, 2015. Each of the 14 plots includes the mean number concentration of the five OPCs against concentration measured by each of the five OPCs during June 5th, 6th and 7th (open circles), standard error of the concentration by the five OPCs during June 5th, 6th and 7th (error bars), linear-least squares regression lines (solid lines), regressed uncertainty range within ± 1 standard deviation (dashed lines), and 1:1 reference line (black dot-dashed line). The seven plots of (B) also include the regressed concentration of each of the five individual OPCs against uncalibrated concentration measured by each of the five individual OPCs during May 29th to June 4th (small closed circles).

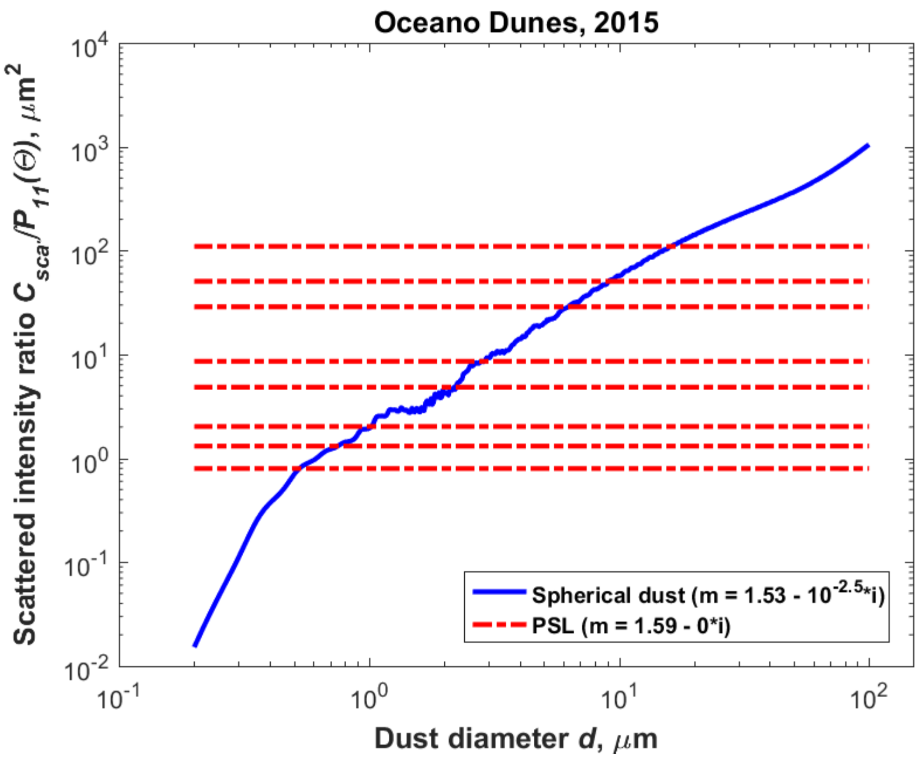

Figure S4. The ratio of scattered light intensity to incident intensity, $C_{sca} \int P_{11}(\Theta)$, as a function of particle diameter using Lorenz-Mie theory. The figure includes the ratios for each of the eight polystyrene latex spheres (PSLs) boundary diameter sizes (red dash-dot lines) (Table 1, column 1) and the ratios for dust particles with various geometric diameters (blue line).

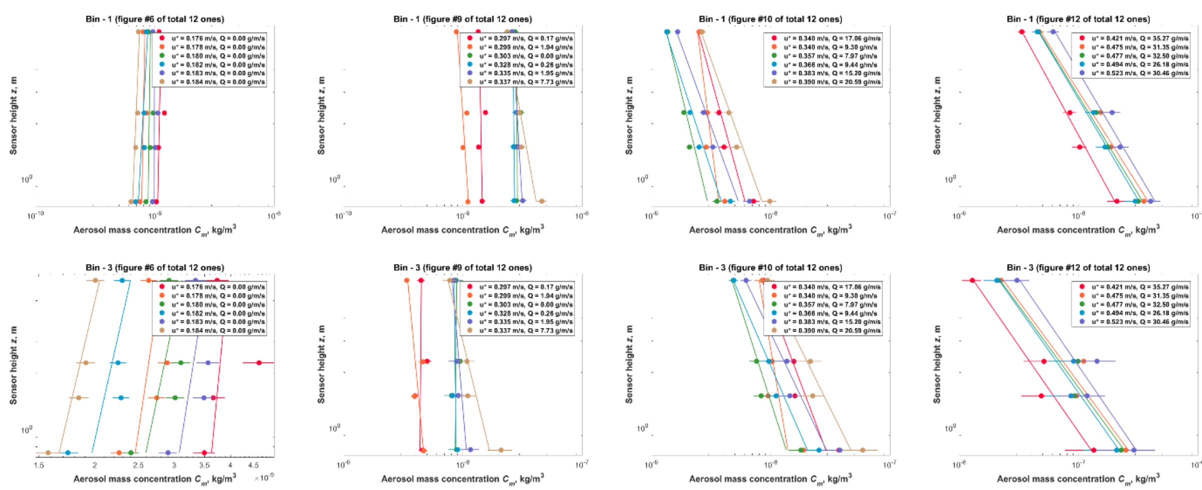

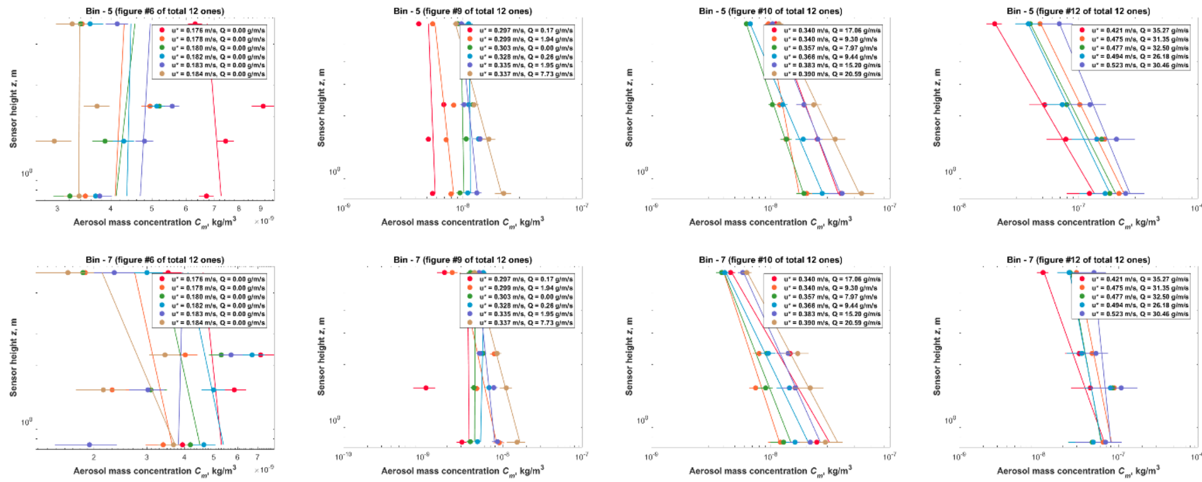

Figure S5. Aerosol mass concentration profiles during May 29th to June 4th, 2015 in order of increasing shear velocity. Each of the 84 subplots (12 subplots * 7 bins) includes the aerosol mass concentrations at four heights (close circles), uncertainties of the mass concentrations (error bars), and linear-least squares regression lines (lines). The value of shear velocity u_* (in the unit of $\mathrm{m/s}$) and the value of horizontal saltation flux Q (in the unit of $\mathrm{g/m/s}$) are provided in the legend. Note that we only present 16 of the 84 subplots due to the limitation in space.

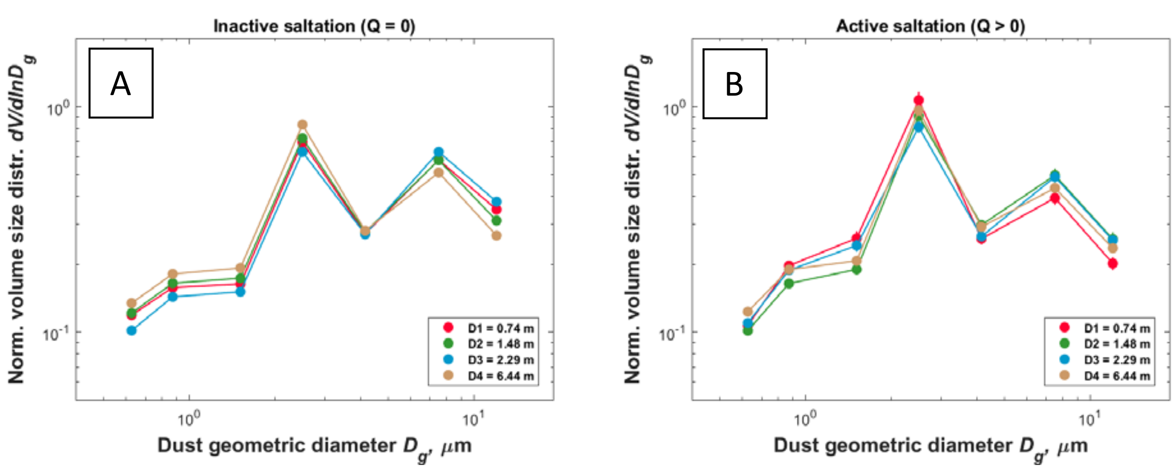

Figure S6. The normalized volume size distribution of aerosol measured at the four OPC heights during May 29th to June 4th, 2015, (A) when saltation is inactive (horizontal saltation flux $\mathrm{Q} = 0$) and (B) when saltation is active ($\mathrm{Q} > 0$).

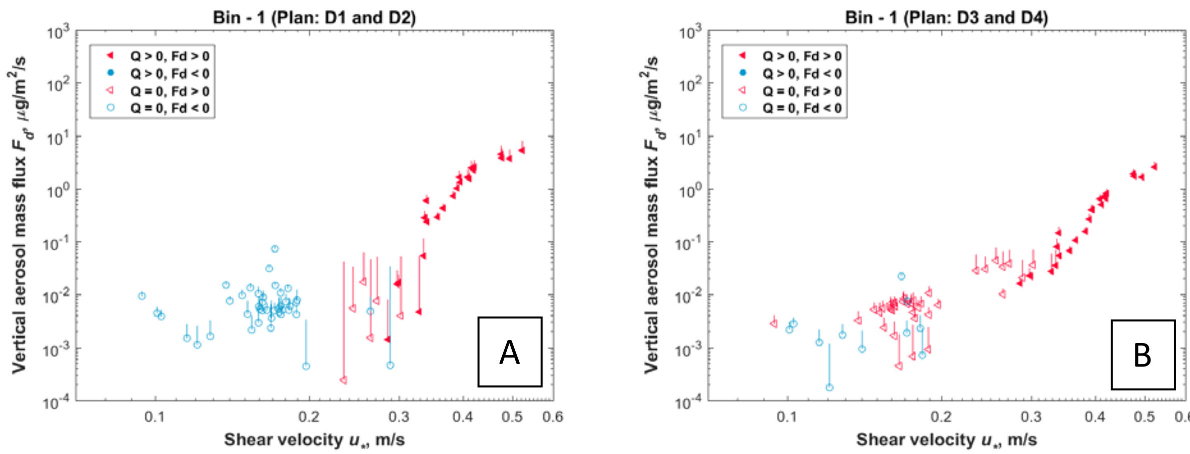

Bin - 1 (Plan: D1 and D2)
Bin - 1 (Plan: D3 and D4)
Q > 0, Fd > 0
Q > 0, Fd < 0
Q = 0, Fd > 0
Q = 0, Fd < 0
Vertical aerosol mass flux F_d, μg/m^2/s
Shear velocity u_*, m/s
A
B

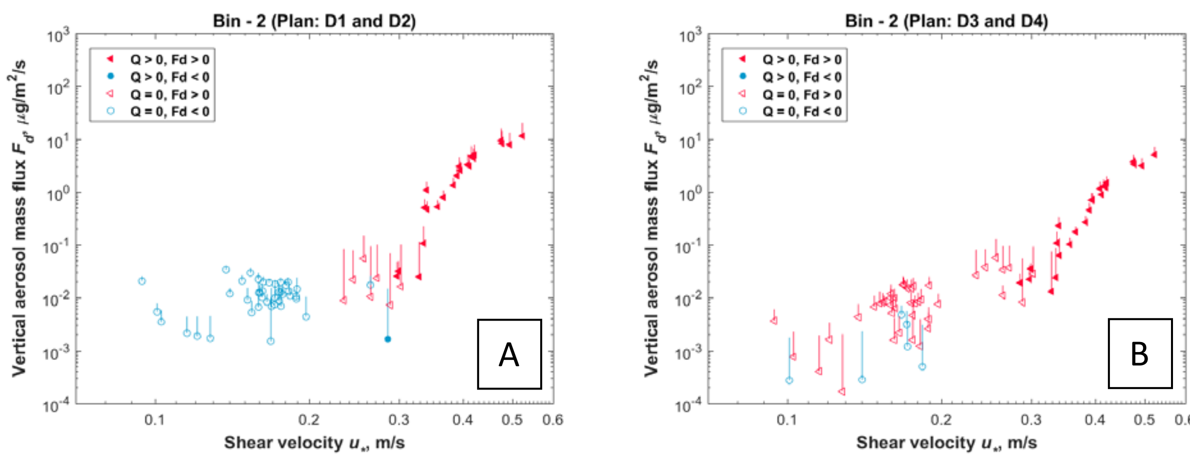

Bin - 2 (Plan: D1 and D2)
Bin - 2 (Plan: D3 and D4)
Q > 0, Fd > 0
Q > 0, Fd < 0
Q = 0, Fd > 0
Q = 0, Fd < 0
Vertical aerosol mass flux F_d, μg/m^2/s
Shear velocity u_*, m/s
A
B

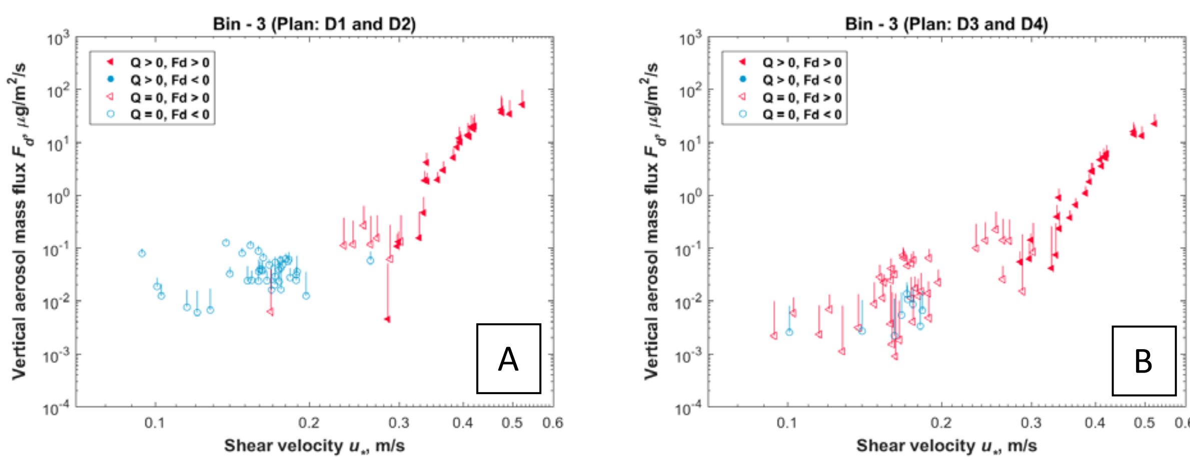

Bin - 3 (Plan: D1 and D2)
Bin - 3 (Plan: D3 and D4)
Q > 0, Fd > 0
Q > 0, Fd < 0
Q = 0, Fd > 0
Q = 0, Fd < 0
Vertical aerosol mass flux F_d, μg/m^2/s
Shear velocity u_*, m/s
A
B

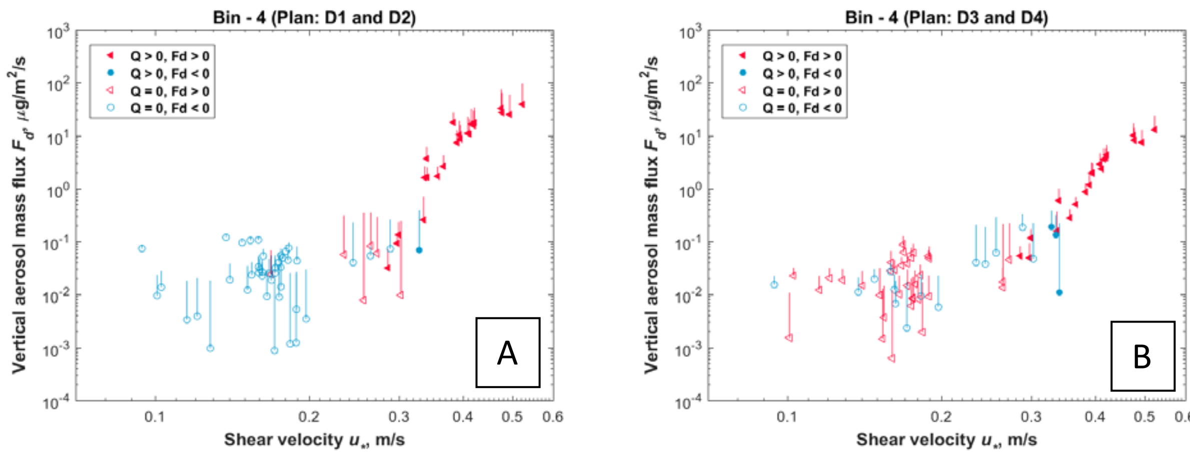

Bin - 4 (Plan: D1 and D2)
Bin - 4 (Plan: D3 and D4)
Q > 0, Fd > 0
Q > 0, Fd < 0
Q = 0, Fd > 0
Q = 0, Fd < 0
Vertical aerosol mass flux F_d, μg/m^2/s
Shear velocity u_*, m/s
A
B

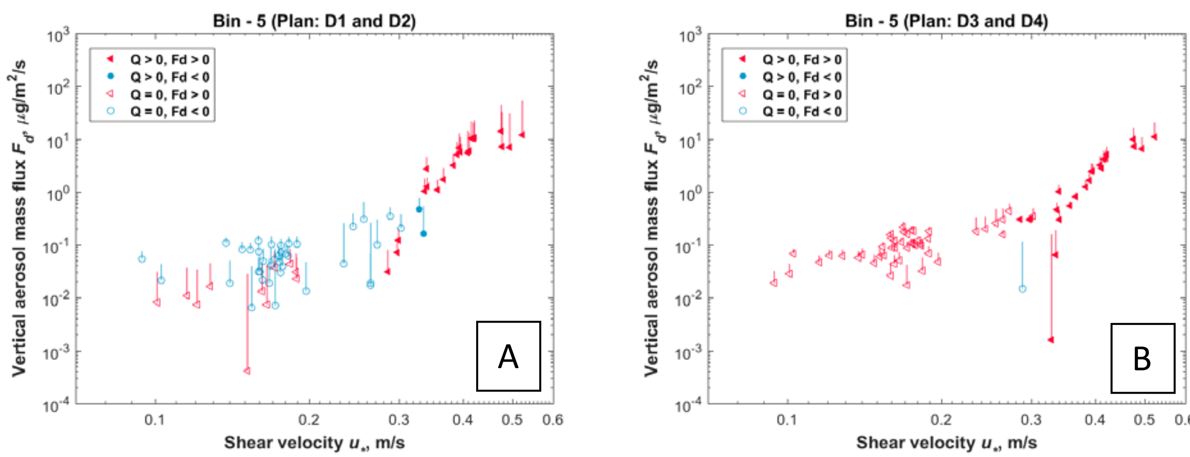

Bin - 5 (Plan: D1 and D2)
Bin - 5 (Plan: D3 and D4)
Q > 0, Fd > 0
Q > 0, Fd < 0
Q = 0, Fd > 0
Q = 0, Fd < 0
Vertical aerosol mass flux F_d, μg/m^2/s
Shear velocity u_*, m/s
A
B

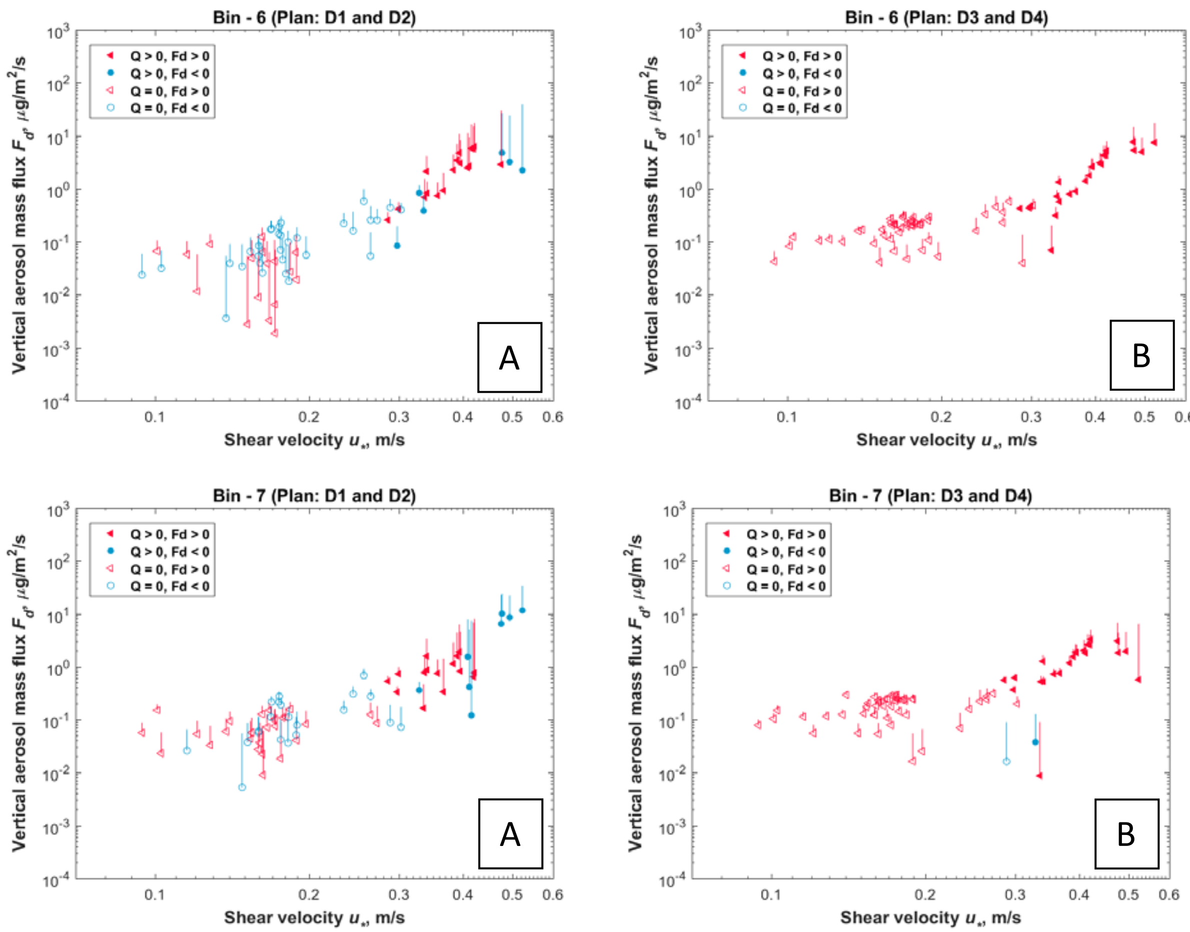

Figure S7. Vertical aerosol mass flux as a function of shear velocity calculated by using two plans of optical particle counters (OPCs)' assemblies during May 29th to June 4th, 2015: (A) using D1 and D2 only, and (B) using D3 and D4 only. Each of the 14 subplots (2 plans * 7 size bins) includes the four scenarios with active saltation and positive flux ($Q > 0, F_d > 0$) (red closed left-pointing triangles), $Q > 0$ and $F_d < 0$ (blue closed circles), $Q = 0$ and $F_d > 0$ (red open left-pointing triangles), and $Q = 0$ and $F_d < 0$ (blue open circles). Uncertainty range (error bars) from error propagation. Note that we plotted the absolute value of negative mass flux under logarithmic scale.

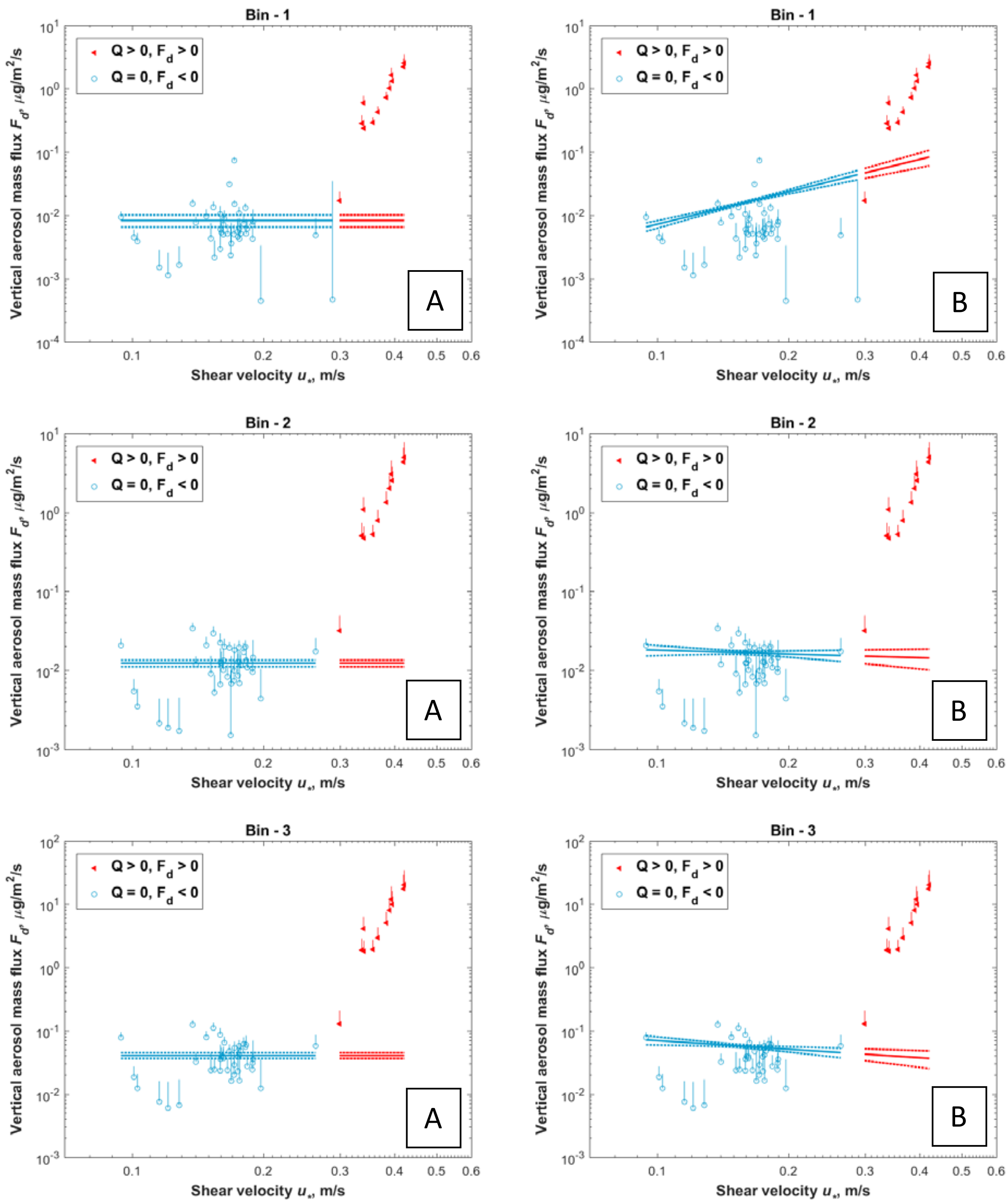
Bin - 1
Bin - 2
Bin - 3
Q > 0, F_d > 0
Q = 0, F_d < 0
Vertical aerosol mass flux F_d, μg/m^2/s
Shear velocity u_*, m/s
A
B

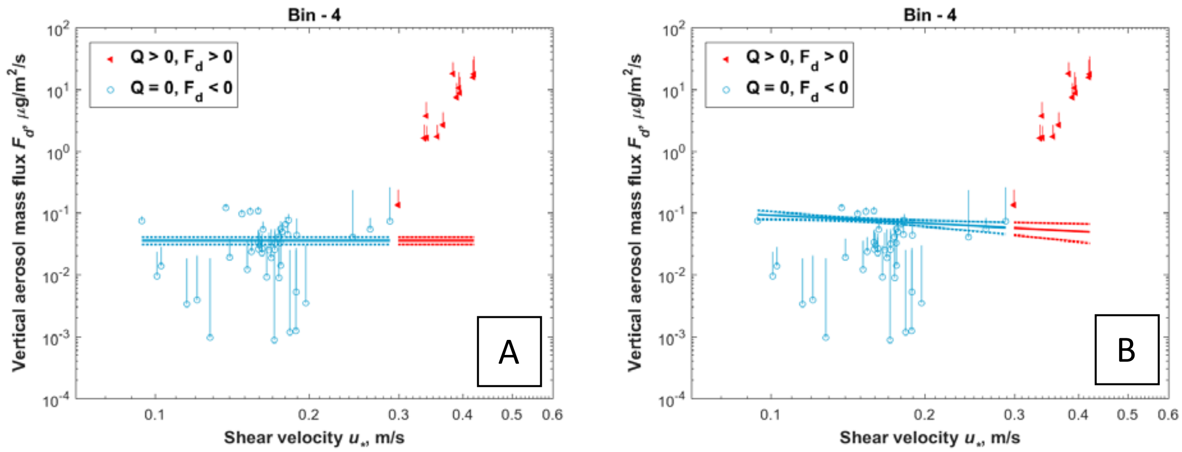
Bin - 4
Q > 0, F_d > 0
Q = 0, F_d < 0
Vertical aerosol mass flux F_d, μg/m^2/s
Shear velocity u_*, m/s
A
Bin - 4
Q > 0, F_d > 0
Q = 0, F_d < 0
Vertical aerosol mass flux F_d, μg/m^2/s
Shear velocity u_*, m/s
B

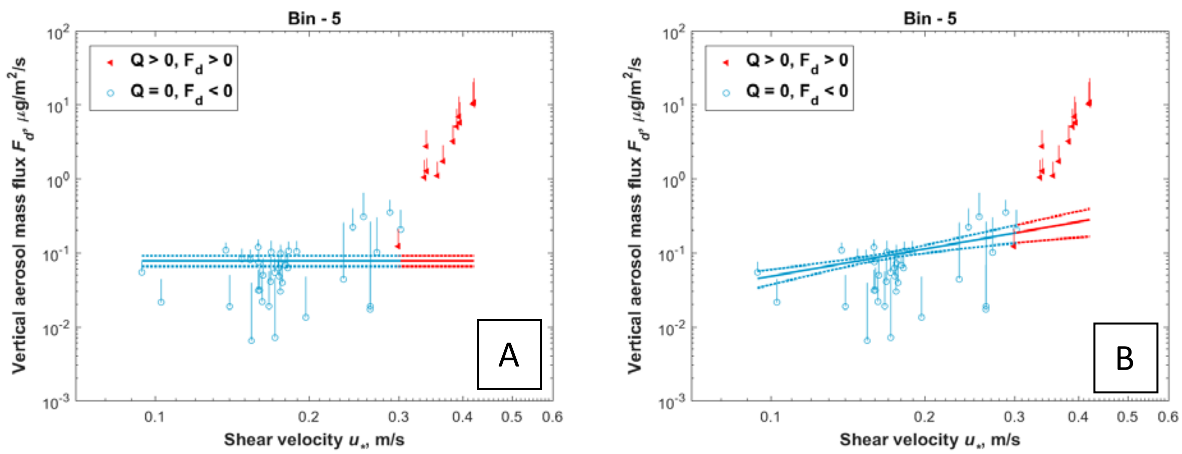
Bin - 5
Q > 0, F_d > 0
Q = 0, F_d < 0
Vertical aerosol mass flux F_d, μg/m^2/s
Shear velocity u_*, m/s
A
Bin - 5
Q > 0, F_d > 0
Q = 0, F_d < 0
Vertical aerosol mass flux F_d, μg/m^2/s
Shear velocity u_*, m/s
B

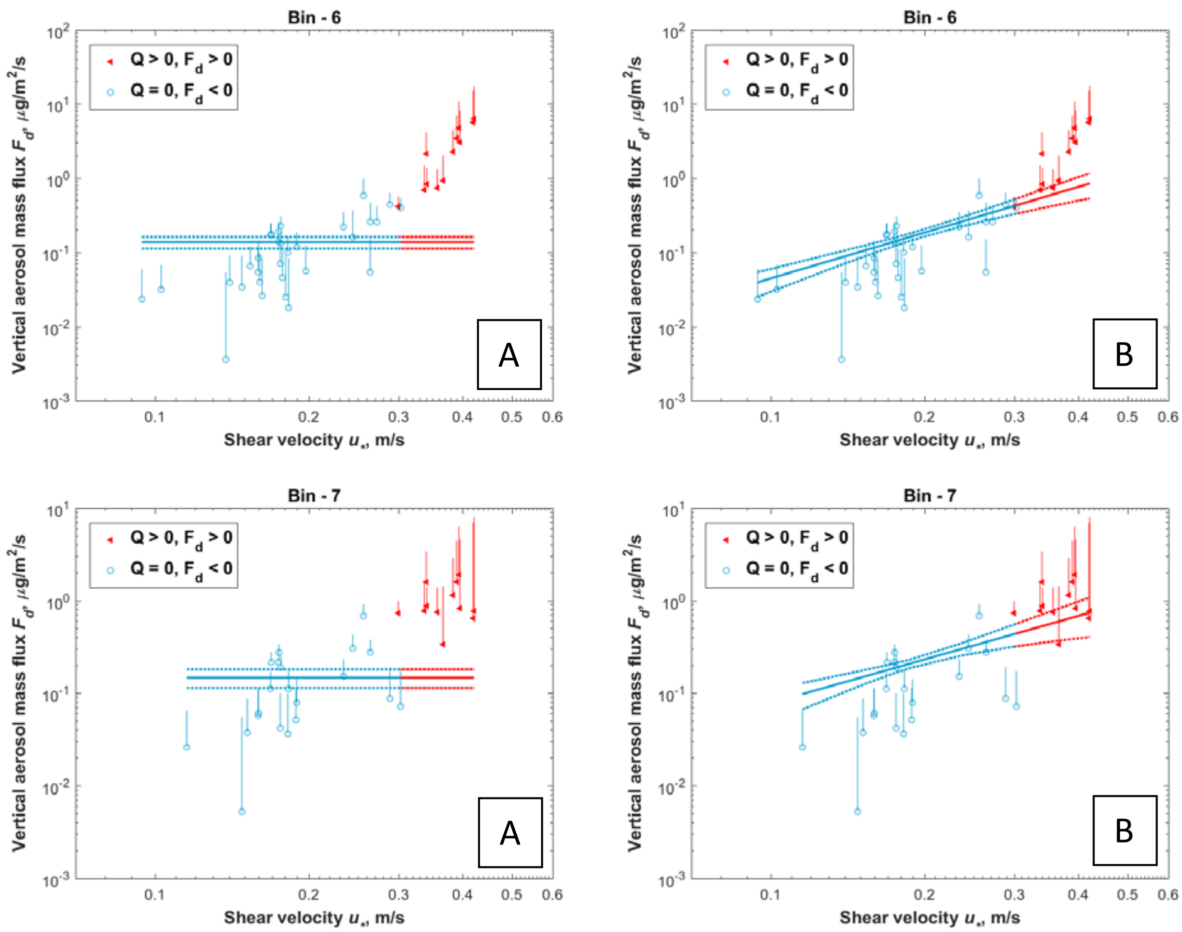

Figure S8. Vertical aerosol mass flux (using D1 and D2 only) as a function of shear velocity during May 29th to June 4th, 2015 using two regression methods: (A) sea-salt deposition flux is invariant with increasing shear velocity, and (B) sea-salt deposition flux increases non-linearly with shear velocity. Each of the 14 subplots (2 methods * 7 size bins) includes the two scenarios with active saltation and positive flux ($Q > 0, F_d > 0$) (red closed left-pointing triangles) and $Q = 0$ and $F_d < 0$ (blue open circles). Uncertainty range (error bars) from error propagation. Note that we plotted the absolute value of negative mass flux under logarithmic scale. Results in the main text used the first regression method (A) to remove the deposition of sea-salt aerosols from our measurements.

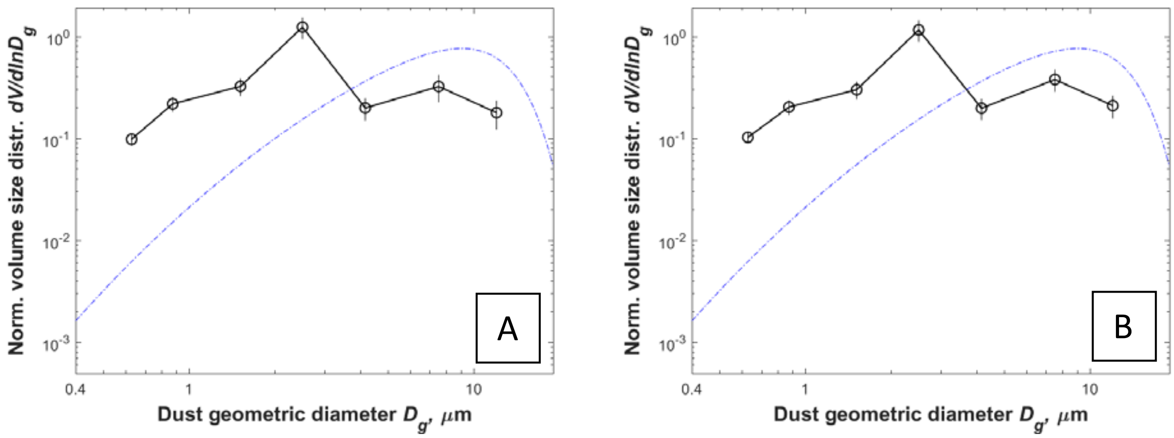

Figure S9. The normalized volume particle size distribution (PSD) of dust at emission using the mass flux calculated by assuming that: (A) sea-salt deposition flux is invariant with increasing shear velocity, and that (B) sea-salt deposition flux increases non-linearly with shear velocity. Also plotted as a reference is the brittle fragmentation theory (blue dash-dotted lines) on the PSD of emitted dust generated by aggregate fragmentation (Kok, 2011).